IEEE Access
Multidisciplinary : Rapid Review : Open Access Journal

Received 12 May 2026, accepted 23 May 2026, date of publication 26 May 2026, date of current version 1 June 2026.
Digital Object Identifier 10.1109/ACCESS.2026.3697150

RESEARCH ARTICLE

A Dual-Functional Frequency-Selective Polarization Converting Metasurface With Reduced Backward-Scattering Characteristics

MUHAMMAD NASIR[1], SLAWOMIR KOZIEL[1,2], (Fellow, IEEE), AND ANNA PIETRENKO-DABROWSKA[2], (Senior Member, IEEE)
[1]Engineering Optimization and Modeling Center, Reykjavik University, 102 Reykjavik, Iceland
[2]Faculty of Electronics, Telecommunications, and Informatics, Gdańsk University of Technology, 80-233 Gdańsk, Poland

Corresponding author: Slawomir Koziel (koziel@ru.is)

This work was supported in part by the Icelandic Research Fund under Grant 2410297, and in part by the National Science Centre of Poland under Grant 2022/47/B/ST7/00072.

ABSTRACT A novel dual-functional frequency-selective metasurface (MS) with low backscattering is proposed by integrating a reflective cross-polarization (LRCP) converter with a bandpass frequency-selective surface (BP-FSS). The proposed MS comprises three layers, with a cross-dipole FSS in the middle layer that provides high-efficiency bandpass transmission. The thickness, inter-gap, and interlayer spacing of the diagonally oriented metallic strip gratings (MSGs), printed on the top and bottom layers, are meticulously optimized to achieve efficient LRCP conversion while maintaining high transmittance transparency for the out-of-band frequencies. The proposed MS simultaneously exhibits two independent functionalities: co-polarized bandpass transmission from 3.74 to 5.12 GHz with a simulated insertion loss of above −1 dB, and LRCP conversion from 5.72 to 7.33 GHz with a polarization conversion ratio (PCR) exceeding 0.99. The design concept is validated using two equivalent circuit models (ECMs) corresponding to the BP-FSS and the cascaded MS configuration, as well as through measurements of the fabricated prototype comprising 16 × 16 unit-cell arrays arranged in a chessboard configuration. Both the ECM predictions and measurements show good alignment with the full-wave simulation findings. In addition, the measurement results showcase significant radar cross-section (RCS) reduction across the frequency range from 5.94 – 7.21 GHz. Unlike conventional LRCP-MSs, the proposed work eliminates the need for a complete ground plane, and hence, its dual functionality makes it a promising candidate for Radome and communication platforms.

INDEX TERMS Radar cross section reduction, linear reflective cross polarization, bandpass FSS, metallic strip gratings, frequency selective surfaces, polarization conversion ratio.

I. INTRODUCTION

The metasurface structures consisting of 2D periodic elements have garnered significant attention in the recent era due to their ability to realize diverse electromagnetic (EM) characteristics [1], [2], [3], [4], [5], [6]. Among them, the LRCP MSs, as a classical approach, have made a significant contribution to RCS reduction, owing to their favorable feature of backscattering suppression through phase cancellation [7], [8], [9], [10], [11], [12], [13], [14]. Various anisotropic LRCP-MSs have been proposed in this regard, such as a diagonal stub loaded with one annular ring embedded with a strip unit [8], two 45° aligned metallic L-shaped resonators [9], notched square ring and rectangular patch elements [10], L-shaped metal patch and a square metal patch unit [11], two pairs of tapered L-shaped strips [12], two C-shaped symmetrical open rings with a central cross-shaped metal structure [13], and a diagonally rotated double-head arrow MS structure [14]. Although these LRCP-MSs aim to reduce RCS, their reliance on a complete conductive

The associate editor coordinating the review of this manuscript and approving it for publication was Bilal A. Khawaja.

ground plane inherently blocks all the incident waves in the transmission mode. This limits their functionality to only reflection-mode operation, curbing all types of transmission functionalities.

Realizing two independent functionalities, including transmission characteristics (i.e., bandpass, bandstop, wavefront, etc.) alongside RCS reduction, remains a key focus for applications such as communication, controlling EM interference for co-located antennas, and Radome [15], [16]. To obtain these features in a single MS design, researchers have proposed a frequency-selective rasorber (FSR) technique, which typically employs BP-FSS to create the transmission window and a resistive sheet or resistor-elements-based surface to reduce the RCS of the out-of-band waves [1], [17], [18], [19]. A recent study on microstrip filter design demonstrates the use of stepped-impedance resonators and open-stub techniques to achieve wide fractional bandwidth and sharp rejection characteristics [20]. The inclusion of a sharp bandpass filter alongside FSR MSs is crucial for achieving improved RCS reduction outside the transmission window. However, a major limitation associated with resistive elements is the increase in the fabrication cost and complexity, and enhancing thermal signatures, which can limit their practicality. Additionally, reduced RCS in FSR structures requires a large number of lumped resistor elements to dissipate EM energy.

Besides the FSR methodology, a cascaded configuration combining coded LRCP-MS and a BP-FSS structure also enables low RCS outside the bandpass window. For instance, a multilayer square patch BP-FSS is placed at the backside of a fishbone-shaped LRCP-MS instead of a conventional metallic ground plane [21]. This configuration achieves co-polarized (co-pol.) bandpass transmission from 8.5 to 11 GHz, along with wideband RCS reduction over 4.5 – 16 GHz. In another approach [22], a cross slot-based BP-FSS is integrated on the backside of an electromagnetic bandgap (EBG) surface by adopting a chessboard arrangement with 0° and 180° reflection phases of the EBG unit cells, a wideband RCS reduction from 8 to 16 GHz is realized, while simultaneously providing a co-pol. bandpass window from 3.9 to 4.3 GHz. Pang et al. [23] adopted a similar reflection-phase technique in the meandered transmission line-based coded MS pattern for RCS reduction. The addition of a multilayer square-patch FSS grid on the backside of the meandered-line MS creates a bandpass window from 8.8 to 10.2 GHz within the wide RCS-reduction band ranging from 4.8 to 17.2 GHz. Similarly, numerous other dual-functionality MS designs that combine RCS reduction with a transmission window have been reported [17], [24], [25], [26], [27], [28], [29].

The aforementioned literature indicates that considerable progress has been made in achieving dual functionality, combining broadband RCS reduction with a bandpass window. Nevertheless, the reflection-mode performance criteria of these structures are strongly dependent on the geometry of the integrated BP-FSS layer. This dependency imposes stringent

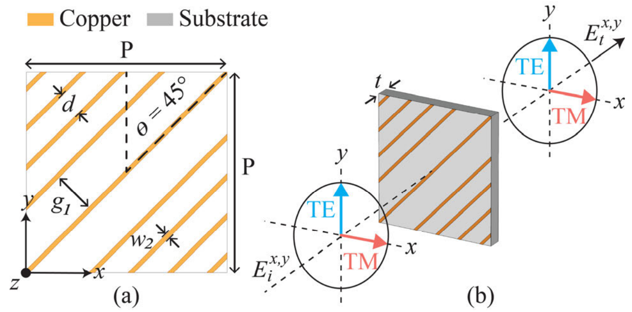

FIGURE 1. (a) MSGs layer, (b) transmission analysis for TE- and TM-polarized incident waves. The dimensions are: [$P = 14$, $d = 2.75$, $g_1 = 3.21$, $w_2 = 0.3$, $t = 1.6$] mm.

constraints on impedance matching and the required phase of decomposed electric-field (E-field) components for effective LRCP conversion. Consequently, two critical issues remain to be addressed:

1. removing the dependency of the LRCP conversion from the BP-FSS geometry.
2. simultaneous and independent realization of bandpass windows and LRCP conversion at different frequency bands. The latter remains largely unexplored even though retaining the LRCP conversion outside the bandpass window has been extensively studied.

Consequently, obtaining independence while simultaneously obtaining bandpass transmission and polarization conversion in reflection at distinct frequency bands is considered an important topic of research.

In this article, a novel compact MS is introduced to achieve wideband LRCP conversion, reducing backward scattering, while maintaining a high-efficiency bandpass at adjacent frequency bands. The MS comprises three layers: the middle layer consists of a BP-FSS, providing a high-efficiency transmission band from 3.74 to 5.12 GHz, while the top and bottom layers incorporate diagonally aligned MSGs forming an angle of 45°, designed to obtain LRCP conversion from 5.72 to 7.33 GHz. In addition, effective monostatic-RCS reduction is observed within the LRCP conversion band when unit cells are arranged in a chessboard configuration. Owing to its two distinct and independent functionalities, the proposed MS may be considered an attractive candidate for applications where low RCS and simultaneous signal transmission at distinct frequency bands are essential.

II. DESIGN EVOLUTION

A. THEORY AND SIMULATION OF MSGs LAYERS

When x- or y-polarized waves impinge on the parallel MSGs (i.e., the MSGs are positioned in the horizontal or vertical directions), it induces surface currents along the MSGs, causing the structure to act primarily as a reflecting surface while allowing the orthogonally polarized waves to transmit through the structure [30], [31], [32], [33], [34]. Applications that require simultaneous control of both polarizations are limited regarding this inherent behavior. To overcome this

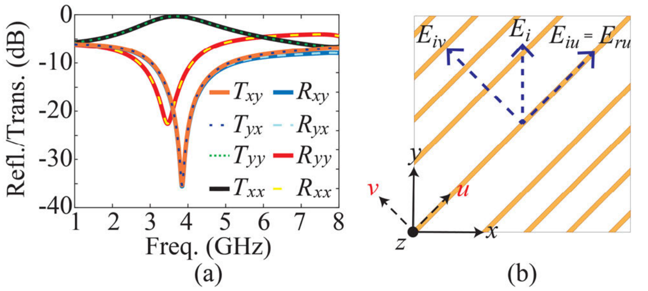

FIGURE 2. (a) Reflective and transmissive co-pol. and cross-pol. components responses of the MSGs layer (b) incident E_i decomposition into *u*- and *v*-components on the MSGs layer.

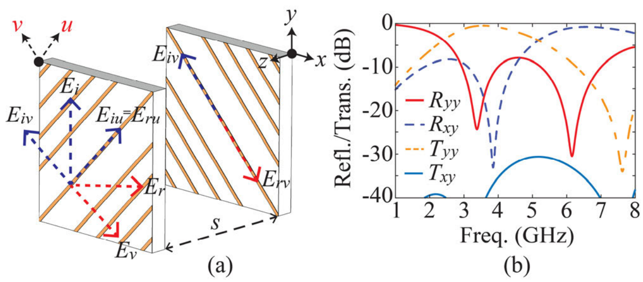

FIGURE 3. (a) Top and bottom MSGs layers separated by the air gap (s) = 6.6 mm, with reflection and transmission of the *u*- and *v*-components on the top MSGs layer, and *v*-component incidence and its reflection from the bottom SGs layer, (b) reflective co-, cross-pol. and transmissive co-, cross-pol. results based on the top and bottom MSGs layers.

limitation, 45° rotated MSGs are introduced on the FR4 substrate ($\varepsilon_r = 4.3$ and $\tan\delta = 0.025$), as shown in Fig. 1(a). To evaluate the transmission mechanism, the MSGs layer is simulated in the CST Microwave Studio using y-polarized (transverse electric, TE) and x-polarized (transverse magnetic, TM) incident waves and are assumed to impinge normally from the $+Z$-direction, as shown in Fig. 1(b). In the following, we denote reflective co- and cross-components as: $R_{yy} = |E_r^y/E_i^y|$, $R_{xy} = |E_r^x/E_i^y|$, transmissive co-components for TE- and TM-polarizations as $T_{yy} = |E_t^y/E_i^y|^{TE}$, $T_{xx} = |E_t^x/E_i^x|^{TM}$, and cross-components as $T_{xy} = |E_t^x/E_i^y|$, and $T_{yx} = |E_t^y/E_i^x|$. Where, E_r^y and E_r^x (E_t^y and E_t^x) are the reflected (transmitted) E-field components along the x- and y-directions, respectively. Whereas E_i^y and E_i^x correspond to E-field excitations in y- and x-directions, respectively.

The simulated reflection and transmission responses of the MSGs layer are plotted in Fig. 2(a). From 2.7 to 4.1 GHz, the T_{xx}, T_{yy} approaches 0 dB, while R_{xx}, R_{yy} remains below -10 dB, confirming the MSGs act as a transmissive surface. However, at a higher frequency range, the reflection magnitude stays around -5 dB, indicating insufficient reflection. Furthermore, no noticeable cross-polarization (cross-pol.) in reflection and transmission is observed throughout the entire band, as both cross-components (R_{xy}, R_{yx}) and (T_{xy}, T_{yx}) magnitudes are around -10 dB.

Noticeably, when E_i of the dual-polarized (dual-pol.) wave impinges normally on the 45° rotated MSGs, it decomposes into two orthogonal u- and v-components [see Fig. 2(b)], as interpreted by the following equation:

$$E_{i,n} = \hat{u}_n E_{iu,n} e^{j\emptyset_{iu,n}} + \hat{v}_n E_{iv,n} e^{j\emptyset_{iv,n}} \tag{1}$$

where n denotes n^{th} MSGs dipole, $E_{iu,n}$ and $E_{iv,n}$ represent the amplitudes of n^{th} component with the corresponding phases $\emptyset_{iu,n}$ and $\emptyset_{iv,n}$.

As seen from Fig. 2(b), the E_{iu} component is aligned parallel to the length of the MSGs, producing surface currents that result in its reflection field, which is expressed as:

$$E_{r,n} = \hat{u}_n E_{ru,n} e^{j\emptyset_{ru,n}} \tag{2}$$

However, the E_{iv} component is orthogonal to the MSGs orientation, thereby producing minimal current, which results in its transmission. Thus, the transmitted component can be written as:

$$E_{t,n} = \hat{v}_n E_{tv,n} e^{j\emptyset_{tv,n}} \tag{3}$$

Here $E_{ru,n}$ and $E_{tv,n}$ are the reflection and transmission coefficients with their respective phases $\emptyset_{ru,n}$ and $\emptyset_{tv,n}$.

It is important to mention that due to the existence of mirror symmetry along the u- and v-axis, the reflection and transmission responses will remain same under dual-pol. incident waves. Therefore, for ease, only the y-polarized (TE-wave) is considered for further analysis and discussions.

Next, to manipulate the transmitted E_{iv} component, another $-45°$ rotated MSGs layer (*bottom layer*) is designed on a similar FR4 substrate and added below to the 45° aligned MSGs layer (*top layer*), as shown in Fig. 3(a). Based on the geometry, the E_{iv} produce surface current, which results in its reflection, given by:

$$E_{r,n} = \hat{v}_n E_{rv,n} e^{j\emptyset_{rv,n}} \tag{4}$$

A complete illustration of the incident and reflected E_i on both MSGs layers is shown in Fig. 3(a). The total reflection (E_r) from the n^{th} MSGs structure combines both decomposed components (E_{iu} and E_{iv}), denoted as:

$$E_r = \hat{u}_n \sum_{n=1}^{N} E_{ru,n} e^{j\emptyset_{ru,n}} + \hat{v}_n \sum_{n=1}^{N} E_{rv,n} e^{j\emptyset_{rv,n}} \tag{5}$$

Eq. (5) incorporates both reflected decomposed components from the top and bottom MSGs layers.

The decomposition of E_i on the top MSGs layer and subsequent reflections from both layers leads to experience a 0° phase shift to one component, same as that to high impedance surface (HIS) behavior. While the second component reflects with a 180° phase shift, indicating perfect electric conducting (PEC) behavior. Thus, a 90° rotation occurs relative to the incident wave, resulting in an LRCP transformation. For efficient LRCP operation, the magnitude of reflected components ($|r_u|$ and $|r_v|$) should be equal to unity, and their phase difference must satisfy $\Delta\phi r_{uv} = |\emptyset r_u - \emptyset r_v| \approx 180^{\circ}$ [35].

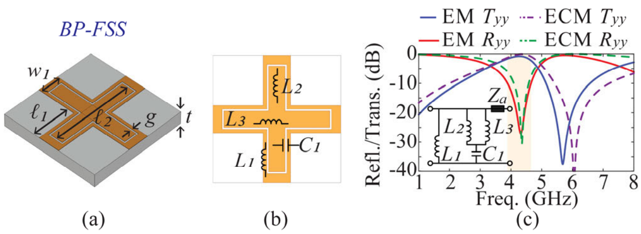

FIGURE 4. (a) Proposed middle layer, with dimension: [w_1 =3, g = 0.2, l_1 = 5.5, l_2 = 11.6, t = 1.6] mm, (b) LC mapping on the CD resonator, (c) transmission and reflection responses comparing full-wave EM simulation with ECM. The lumped element values are: L_1 = 4.32 nH, $L_2 = L_3$ = 10.84 nH, and C_1 = 0.13 pF.

Fig. 3(b) shows the simulated results of the combined top and bottom MSGs layers, revealing that the combined layers exhibit LRCP conversion between 5.24 – 7 GHz, having R_{xy} value ranging from −3.5 to −1 dB and corresponding R_{yy} is below −10 dB. Furthermore, no effective LRCP conversion is observed below 5.25 GHz, as the R_{xy} value gradually drops below −10 dB. Besides, negligible cross-pol. transmission T_{xy} is observed across the entire frequency range as its magnitude stays below −30 dB.

Here two important observations can be made based on the MSGs layers simulation results:

1. Around 0 dB transmission magnitude is observed in between 2 – 5 GHz, indicating that the two MSGs layers remain transparent to the incident wave in this region.
2. The T_{yy} magnitude is observed around −5 dB from 5.25 to 6 GHz, demonstrating the occurrence of partial co-pol. transmission within the LRCP range.

These observations imply that the LRCP performance can be further improved, and the transparent region (between 2 – 5 GHz) can be utilized for the transmission functionality.

B. BANDPASS FSS LAYER

A BP-FSS layer incorporating a cross-dipole (CD) structure on the FR4 substrate [see Fig. 4(a)] is utilized to evaluate the transmittance transparency of the proposed MSGs layers. The BP-FSS structure is rotationally symmetric and thereby exhibits a similar response under dual-pol. Thus, upon E-fields incidence, the induced surface current on the CD arms forms the inductive effect, which is modeled by the inductor L_1, L_2, and L_3, respectively. While the capacitive C_1 effect originate from the induced coupling across the physical gap. The center frequency f_0 of the BP-FSS can be calculated as $f_0 = 1 \Big/ 2\pi\sqrt{LC}$ [36]. The mapping of LC elements onto the CD resonator is illustrated in Fig. 4(b), while the inset of Fig. 4(c) presents the complete ECM. The substrate is modeled as transmission lines with impedance $Z_a = Z_0/\sqrt{\varepsilon_{eff}}$ [2]. where Z_0 is the impedance of free space (i.e., 120π). It can be observed from Fig. 4(c) that the derived ECM model results corroborate with the full wave EM simulation results. The final optimized values of the LC components are mentioned in the caption of Fig. 4.

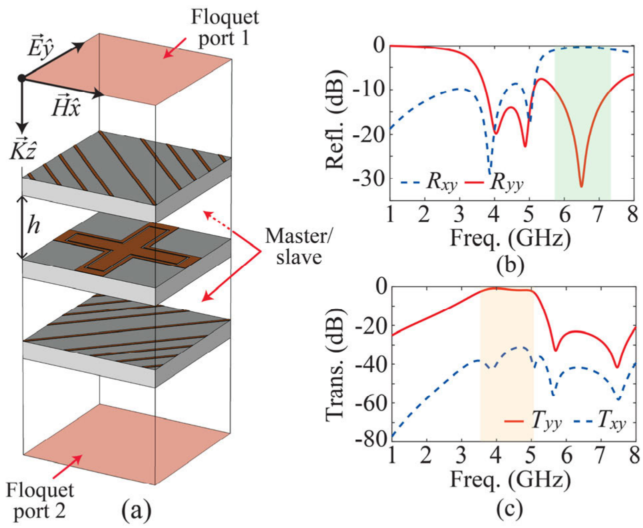

FIGURE 5. (a) Perspective view of the complete unit cell structure, (b) co-pol. and cross-pol. reflection response, (d) and co-pol. and cross-pol. transmission response of the proposed MS unit cell.

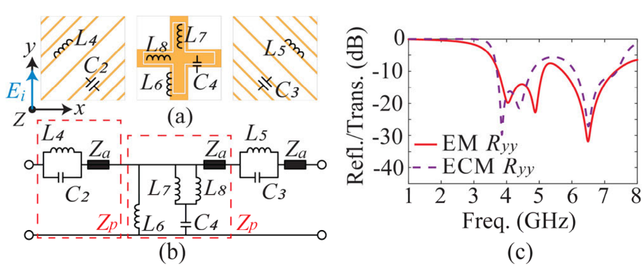

FIGURE 6. (a) Mapping of the LC components onto each surface layer, (b) complete ECM of the cascaded MS, (c) co-pol. reflection comparison of the full wave EM simulation and the derived ECM model. The optimized LC values are: $L_4 = L_5$ = 22.55 nH, $C_2 = C_3$ = 0.2 pF, L_6 = 1 nH, L_7=L_8 = 0.92 nH, C_4 = 0.53 pF.

C. INTEGRATED MS DESIGN

Finally, the BP-FSS structure is inserted between the top and bottom MSGs layers, maintaining an interlayer separation of h = 4 mm, forming the proposed MS design, as shown in Fig. 5(a). Based on the multiple-interference theory [37], the proposed tri-layer structure acts as a Fabry-Pérot-like cavity, supporting multiple reflections and transmissions. Consequently, favoring the destructive co-pol. conversion and constructive cross-pol. conversion. As a result of constructive interference, a wide frequency bandwidth with high-purity LRCP conversion is achieved. It is evident in Fig. 5(b) that the performance of LRCP is improved in the frequency band of 5.72 – 7.33 GHz, wherein the R_{xy} < −1 dB and R_{yy} is below −10 dB. While Fig. 5(c) shows that, in the 3.74 – 5.12 GHz range, the bandpass insertion loss is above −1 dB and corresponding reflection R_{yy} magnitude remains under −10 dB, validating the bandpass characteristics. Notably, the T_{yy} value decays below −10 dB within the LRCP conversion band, ensuring the effective LRCP performance of the proposed MS. Owing to the Fabry-Pérot cavity effect in the proposed tri-layer structure, a very weak

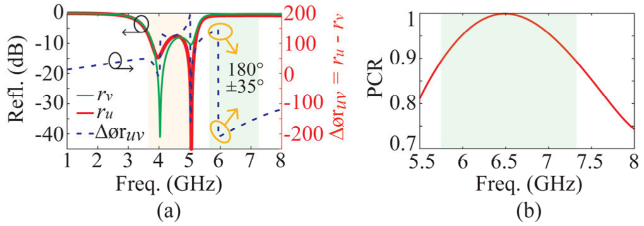

FIGURE 7. (a) Reflection magnitude and phase difference ($\Delta\phi r_{uv}$) of the u- and v-components, (b) PCR across the LRCP conversion band.

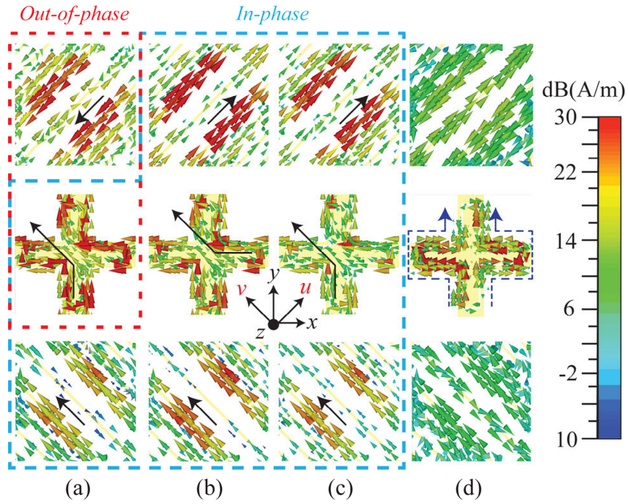

FIGURE 8. Surface current distribution on the top layer (*first row*), middle layer (*second row*), and bottom layer (*third row*), at the resonant frequencies of: (a) 6 GHz, (b) 6.5 GHz, (c) 7 GHz, and (d) 4.4 GHz.

transmissive cross-pol. conversion appears throughout the entire frequency band, with T_{xy} magnitude reaching -30 dB, which is sufficiently small enough to be ignored. In summary, the proposed MS simultaneously achieves two independent functionalities, including LRCP conversion in the C-band and a bandpass window covering the S-band and a small portion of the C-band.

To further elucidate the co-pol. reflection R_{yy} response of the proposed tri-layer configuration, an ECM is derived using *LC* components. Fig. 6(a) depicts the *LC* mapping onto each surface layer of the MS unit cell. The metallic strips on the top and bottom layers contribute to inductances (L_4, L_5), while their inter-gap gives rise to capacitance (C_2, C_3). The equivalent inductance (L_e) and capacitance (C_e) associated with the cascaded design can be derived using $L_e = \frac{\sqrt{\varepsilon_{\text{eff}}} * Z_c * l}{c}$ and $C_e = \frac{\sqrt{\varepsilon_{\text{eff}}} * l}{c * Z_c}$ [38]. Where ε_{eff} is the effective permittivity, l represents the line length, Z_c denotes the characteristic impedance, and c is the speed of light. Here, Z_c of the metallic pattern embedded dielectric substrates and airgap can be identified as Z_a and Z_p respectively. Following this, a complete ECM of the proposed MS is modeled, as shown in Fig. 6(b), while Fig. 6(c) demonstrates a close resemblance between full-wave EM simulation and derived ECM results. Furthermore, the optimized values of the *LC* component are mentioned in the caption of Fig. 6.

Other notable parameters for interpreting the LRCP mechanism include the u- and v-components and their phase difference analysis. According to the proposed MS geometry, the non-existence of isotropy along the u- and v-axis, where one decomposed component reflects and acts as a HIS, while the second component acts as a PEC, consequently leading to 180° phase difference. From Fig. 7(a), the magnitudes of the reflected components satisfy $|r_u| = |r_v| \approx 1$ and $|\emptyset r_u - \emptyset r_v| = \Delta\phi r_{uv} \approx 180^\circ \pm 35^\circ$ within the LRCP conversion band from 5.72 – 7.33 GHz. Besides, due to the frequency-dependent nature of the MS, the magnitude of the decomposed components stays below -5 dB and $\Delta\phi r_{uv}$ remains between 110° – 200° in the bandpass (3.74 – 5.12) region. Thereby, the polarization state of the E_i remains unchanged.

To further evaluate the purity of the LRCP conversion, we define PCR using the linear reflection magnitudes as stated; $\text{PCR} = (R_{xy}^2/(R_{xy}^2 + R_{yy}^2))$ [35]. Fig. 7(b) reveals that, in the LRCP conversion band (5.72−7.33 GHz), the PCR retains a peak value exceeding 0.99. The near-unity PCR magnitude reveals a perfect LRCP conversion.

To counter verify the HIS and PEC characteristics, a current distribution analysis is performed on each surface layer at the resonant frequencies of 6 GHz, 6.5 GHz, 7 GHz, and 4.4 GHz, and illustrated in Figs. 8(a) – 8(d), respectively. At 6 GHz [Fig. 8(a)], the current vectors on the top layer are directed downward along the $-u$-direction. While the current on the middle layer is orthogonal to the top layer in the v-direction. These out-of-phase current vectors lead to a strong magnetic resonance, causing the surface to function as HIS. In contrast, the in-phase current direction on the middle and bottom layers results in a PEC response. At 6.5 GHz and 7 GHz [Figs. 8(b) and 8(c)], the currents on the top and middle layers remain orthogonal; however, their in-phase current leads to a PEC response. Additionally, in-phase currents on the middle and bottom layers produce strong electric resonance loops, enabling the MS to act as a PEC. Notably, the surface current is primarily concentrated on top and bottom MSGs, highlighting their contribution to the LRCP response.

Moreover, the surface current distribution analysis is performed at the bandpass frequency of 4.4 GHz [Fig. 8(d)], revealing that the dominant in-phase currents are mainly confined the CD resonator edges, inducing a bandpass response from 3.74 to 5.12 GHz. Meanwhile, the out-of-phase current is observed along the y-direction, indicating a current-cancellation (null) effect in that direction. Notably, at 4.4 GHz, the current vectors' magnitude on the top and bottom MSGs layers remains minimal, indicating their negligible contribution to the bandpass response.

A conclusion drawn from the above analyses is that the proposed MS holds two independent functionalities. One is the LRCP conversion, which is mainly controlled by the interaction of the decomposed u- and v-components on the MSGs

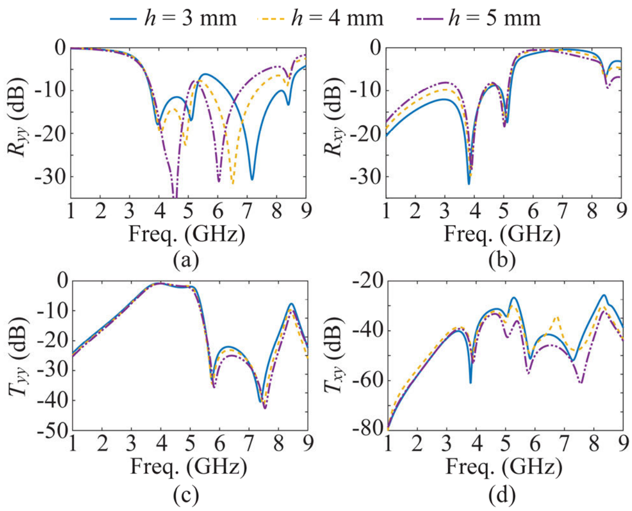

FIGURE 9. Reflection and transmission responses of varying inter-layer spacing: (a) R_{yy}, (b) R_{xy}, (c) T_{yy}, and (d) T_{xy}.

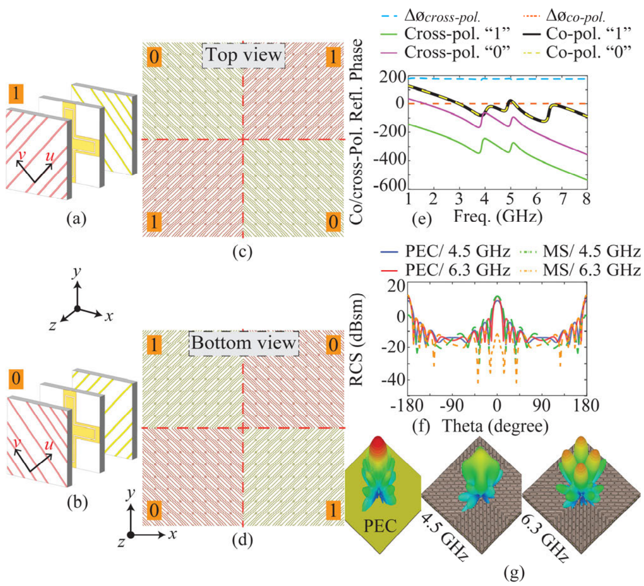

FIGURE 10. Chessboard array configuration for RCS reduction composed of 16 × 16 unit cells: (a) unit cell design ("1"), (b) mirror unit cell ("0"), (c) top view of array sections showing ("1") and ("0") arrangement, (d) bottom view of array sections showing ("0") and ("1") arrangements, (e) co- and cross-pol. reflection phase responses of unit cells "0" and "1" and their corresponding phase differences, (f) simulated Cartesian far-field scattering patterns for PEC plate and proposed chessboard array under normal incidence for 4.5 GHz and 6.3 GHz, (g) 3D monostatic RCS pattern of the reference PEC plate and proposed chessboard array for 4.5 GHz and 6.3 GHz.

layers. Second, CD resonator geometry determines bandpass behavior. These responses can be mathematically expressed through Jones matrix [39]. In the reflection mode, the co- and cross-polarized reflection coefficients can be described as:

$$\begin{bmatrix} E_{rx} \\ E_{ry} \end{bmatrix} = \begin{bmatrix} R_{xx} & R_{xy} \\ R_{yx} & R_{yy} \end{bmatrix} \begin{bmatrix} E_{ix} \\ E_{iy} \end{bmatrix},$$

If the following condition for LRCP is satisfied: $|R_{xx}| = |R_{yy}| \approx 0$, and $|R_{xy}| = |R_{yx}| \approx 1$, then reflection matrix can be derived based on the simulation parameters:

$$\begin{bmatrix} 0.02 & 0.95 \\ 0.95 & 0.02 \end{bmatrix}^{+z} \approx \begin{bmatrix} 0 & 1 \\ 1 & 0 \end{bmatrix}^{+z}.$$

While in the transmission mode, the simulated bandpass transmission can be approximated as:

$$\begin{bmatrix} E_{tx} \\ E_{ty} \end{bmatrix} = \begin{bmatrix} T_{xx} & T_{xy} \\ T_{yx} & T_{yy} \end{bmatrix} \begin{bmatrix} E_{ix} \\ E_{iy} \end{bmatrix} \approx \begin{cases} \begin{bmatrix} 0 & 0.01 \\ 0 & 0.91 \end{bmatrix}^{+z}_{y-pol.} \\ \begin{bmatrix} 0.91 & 0 \\ 0.01 & 0 \end{bmatrix}^{+z}_{x-pol.} \end{cases} \approx \begin{bmatrix} 1 & 0 \\ 0 & 1 \end{bmatrix}^{+z}_{x-,y-pol.}$$

These matrices for both reflective (transmissive) coefficients underscore that the cross-components are approximately equal to one (zero) while co-components are nearer to zero (one), thereby validating the independent responses, including LRCP conversion (bandpass) functionalities.

It is noticed that the inter-layer spacing (h) directly affects the coupling strength and phase behavior of the transmitted and reflected decomposed u- and v-polarized wave components, thereby controlling the LRCP conversion performance. To examine this effect, spacing (h) thickness varies, and the generated effects on co- and cross-pol. reflected and transmitted components are presented in Figs. 9(a) – 9(d). At a 3 mm spacing [Fig. 9(a)], the R_{yy} bandwidth expands from 6.31 to 8.3 GHz (27.24%) due to the presence of strong inter-layer EM coupling and multiple-interference effects. In contrast, weak coupling at 5 mm spacing yields a narrow bandwidth from 5.47 to 6.77 GHz (21.24%). Additionally, the corresponding R_{xy} values remain above −1 dB, as depicted in Fig. 9(b). Besides, a minor impact on the bandpass bandwidth is observed by varying the spacing, whereby it retains ≈ −1 dB insertion loss from 3.74 to 5.12 GHz, as seen in Fig. 9(c). Meanwhile, the cross-component T_{xy} magnitude stays below −20 dB thought the designated band, denoting the absence of cross-pol. in transmission, as depicted in Fig. 9(d). Conclusively, adjusting the inter-layer spacing enables the MS to control the LRCP bandwidth without affecting the bandpass functionality.

III. APPLICATION OF THE LRCP CONVERSION FUNCTIONALITY TO RADAR CROSS-SECTION REDUCTION

In addition to LRCP conversion and bandpass functionality, the proposed MS also reduces RCS through phase cancellation. This is valuable for stealth enhancement in radomes and antenna structures. To examine the RCS-reduction effect, the MS unit cell structures are organized in a chessboard configuration, with unit cell "1" and its mirror structure "0" in four quadrants, in a 10/01 sequence, as depicted in Figs. 10(a) – 10(d), respectively. Each quadrant has 8 × 8 unit cells, totaling a physical dimension of 224 × 224 mm^2 for accurate sampling of the scattering characteristics. The monostatic RCS (σ_{MS}) of the

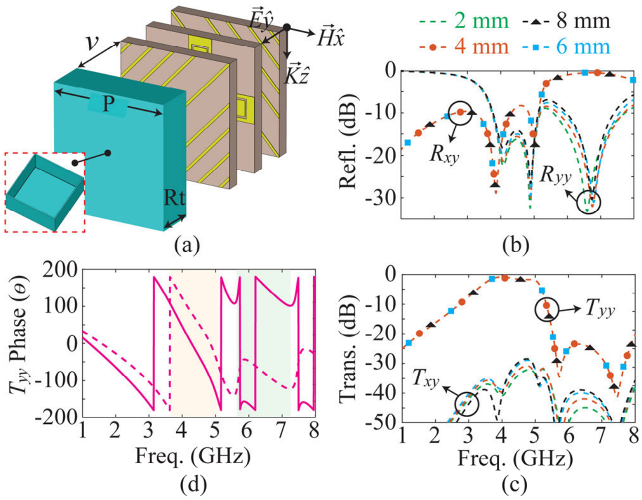

FIGURE 11. (a) Integration of the DR cover with the proposed MS structure, (b) co-pol. and cross-pol. reflection, (c) co-pol. and cross-pol. transmission, (d) and co-pol. transmission phase response of the proposed MS unit cell with (*dotted line*) and without Radome (*solid line*) integration.

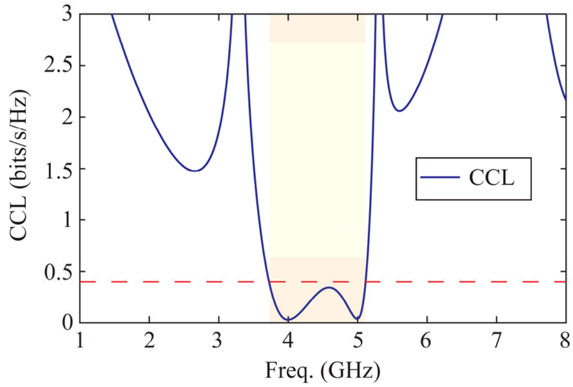

FIGURE 12. Calculated CCL of the proposed MS.

MS can be calculated using [40]:

$$RCS_{reduction} = 4\pi R^2 \left(\frac{\left|\vec{E}_{ry}\right|^2}{\left|\vec{E}_{iy}\right|^2} \right) \tag{6}$$

where R denotes the observation distance in the far-field region, $\vec{E}_{iy}$ represents the incident E_i, and $\vec{E}_{ry}$ corresponds to the scattered E_i component observed in the backward direction. For the chessboard configuration, the RCS reduction relative to a PEC plate of identical dimensions follows [13], [21], [40], and [41]:

$$RCS_{reduction} \approx 10 \log_{10} (1 - PCR). \tag{7}$$

Eq. (7) provides an approximate estimation of the monostatic RCS reduction behavior associated with the LRCP conversion-based unit cells and their corresponding phase-cancellation mechanism. In the proposed chessboard configuration, both unit cells and their mirrored (i.e., "0" and "1") generate nearly 180° phase differences in the cross-polarized reflected fields, leading to destructive interference in the backward direction and consequently reduced backward-scattering.

To verify the backscattering performance, a y-polarized plane wave propagating in the $+Z$-direction is used to excite the chessboard. Fig. 10(e) reveals that the chessboard array achieves 180° phase difference ($\Delta\phi$) for cross-pol. and 0° for the co-pol. components through a "0" and "1" unit cells arrangement, resulting in backward phase cancellation and monostatic RCS reduction.

The Cartesian far-field 2D scattering patterns and 3D radiation patterns in Figs. 10(f) and 10(g) compare the reference PEC plate and proposed chessboard response at 4.5 GHz (*bandpass*) and 6.3 GHz (*LRCP conversion*), respectively. At both frequencies, the PEC plate exhibits a prominent specular lobe in the boresight direction ($\theta = 0°$), as stated by Snell's law of reflection. However, due to MS's transmissive behavior at 4.5 GHz, phase cancellation is prevented, resulting in a specular reflection. In contrast, the chessboard pattern at 6.3 GHz reduces backscatter by over 10 dB compared to the PEC reference, due to the 180° phase variations between "0" and "1" unit cells. These results confirm that the presented design is robust and reduces RCS only in the LRCP band.

Notably, the proposed MS achieves RCS reduction in the LRCP conversion band via phase cancellation. However, due to the symmetric geometry of the BP-FSS layer, the required phase variation cannot be achieved, leading to residual specular reflection. This reflection can be suppressed by incorporating FSR MSs [17], [18], [19] or additional phase-cancellation layers [22], [23]. However, the inclusion of such layers may increase insertion loss, bulkiness, complexity, and degrade performance.

IV. PERFORMANCE ANALYSIS OF DUAL FUNCTIONALITY TO RADOME AND COMMUNICATION APPLICATIONS

To validate the suitability of dual-functionality to the purposed applications, a simulation-based analysis has been carried out by introducing a dielectric Radome (DR) with dimensions [$P = 14$, $Rt = 5$] mm in front of the MS. Considering fabrication simplicity and mounting flexibility, the square DR is selected, as shown in Fig. 11(a). A polycarbonate material for DR with relative permittivity $\varepsilon_r = 3$ and tan$\delta = 0.01$ is considered and placed at a distance (v). To achieve lower insertion loss, the DR is designed with a thin wall thickness of 0.5 mm. When v varies from 2 mm to 8 mm, the co-pol. and cross-pol. reflection R_{yy}, R_{xy} and transmission T_{yy}, T_{xy} coefficients remain almost unchanged, as validated from Figs. 11(b) and 11(c), respectively. These results demonstrate that the inclusion of Radome introduces only minor variations in both the LRCP conversion and band-pass transmission characteristics.

Furthermore, the transmission phase response in the pass-band is analyzed to evaluate the impact on the wavefront. As shown in Fig. 11(d), the transmission phase remains

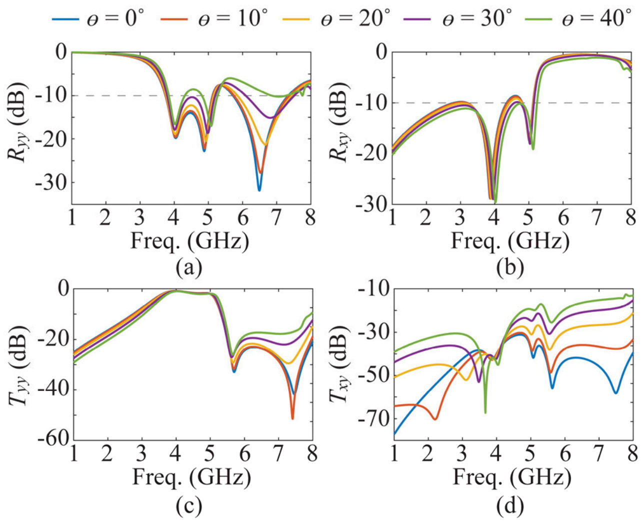

FIGURE 13. Simulated responses of the proposed MS under varying incident angles. (a) co-pol. reflection, (b) cross-pol. reflection, (c) co-pol. transmission, and (d) cross-pol. transmission.

stable, with negligible deviations, after the DR cover integration. This stable phase behavior ensures minimal distortion of the transmitted wavefront, which is essential for Radome to avoid beam degradation, boresight shift, and gain reduction.

Besides, to gain more insight into the communication capability of the proposed MS, the channel capacity loss (CCL) is evaluated. The CCL serves as a figure of merit to quantify the reduction in the maximum achievable transmission rate in the communication channel. For the dual-polarized MS, the CCL is derived as [42]:

$$CCL = -\log_2^{|\psi^R|} \tag{8}$$

$$\psi^R = \begin{bmatrix} \rho_{yy} & \rho_{yx} \\ \rho_{xy} & \rho_{xx} \end{bmatrix} \tag{9}$$

$$\rho_{yy} = 1 - \left(|R_{yy}|^2 + |R_{yx}|^2\right) \tag{10}$$

$$\rho_{yx} = -\left(R^*_{yy}R_{yx} + R^*_{xy}R_{xx}\right) \tag{11}$$

$$\rho_{xy} = -\left(R^*_{xx}R_{xy} + R^*_{yx}R_{yy}\right) \tag{12}$$

$$\rho_{xx} = 1 - \left(|R_{xx}|^2 + |R_{xy}|^2\right) \tag{13}$$

The calculated CCL is presented in Fig. 12. It is observed that the CCL value remains below the acceptable threshold of 0.4 bits/s/Hz within the bandpass region, indicating efficient transmission with minimal capacity loss. Conversely, around 2 bits/s/Hz are observed outside the bandpass region, corresponding to signal degradation due to the MS's dominant reflective behavior. In conclusion, the proposed MS is well-suited for transparent communication only in the bandpass region. It should be noted that the presented DR cover and transmission-phase analyses provide only a preliminary feasibility assessment for radome integration. Comprehensive practical radome validation would also require investigations involving environmental conditions (e.g., humidity, temperature, etc.), structural loading effects, and antenna-integrated radiation performance, which are beyond the scope of the present work.

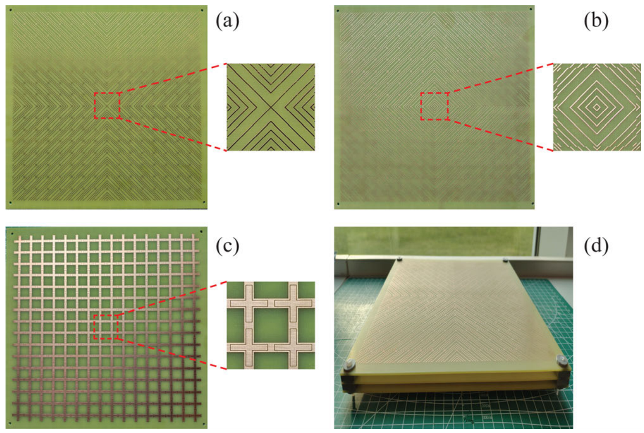

FIGURE 14. Fabricated prototype of the proposed MS array, (a) top layer, (b) bottom layer, (c) middle layer, and (d) assembled prototype.

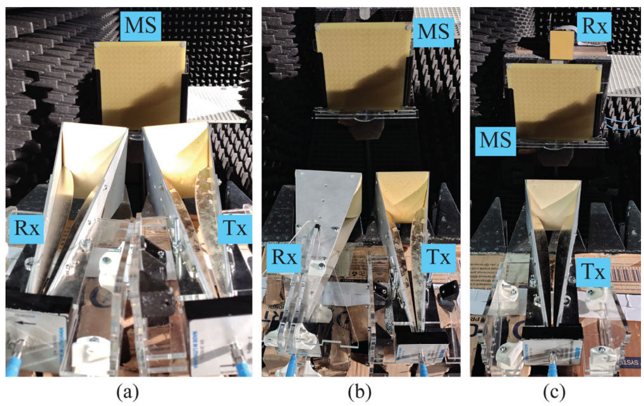

FIGURE 15. Adopted experimental setup comprising MS, T_x, and R_x antennas for (a) co-pol. reflection (b) cross-pol. reflection, and (c) bandpass measurements.

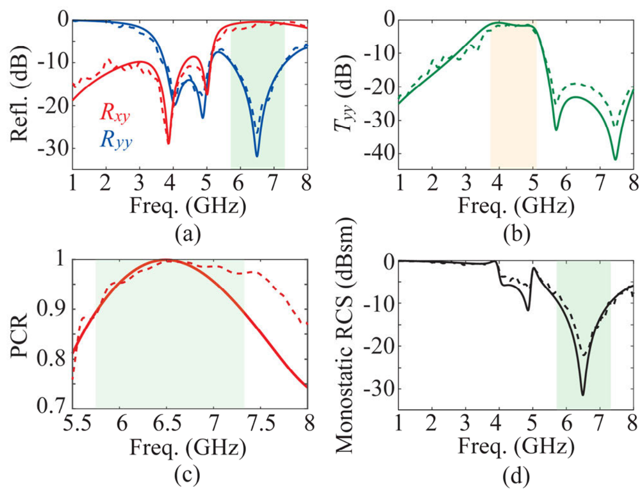

FIGURE 16. Comparison of the simulated (*solid lines*) and measured (*dotted lines*) responses of (a) co- and cross-pol. reflection (b) co-pol. transmission, (c) PCR, (d) monostatic RCS reduction of proposed chessboard configuration.

In addition to DR and CCL analysis, the dual functionality of the proposed MS is further evaluated under oblique incident angles, as presented in Fig. 13. Upon E_i the R_{yy} bandwidth started to deteriorate from approximately 30° [Fig. 13(a)], due to the spatial dispersion effect. Increasing the incident angle increases the electrical length of the period, resulting in spatial dispersion [35], [43], [44]. This dispersion causes a frequency shift, introduces additional parasitic resonance, and alters the phase response, thereby affecting overall performance. This effect is also observed in Fig. 13(b), where the R_{xy} magnitude decays below −3 dB at 40° in the LRCP conversion band. For T_{yy}, its magnitude stays near −1 dB [Fig. 13(c)] at the designated bandpass range. Moreover, the T_{xy} stays below −10 dB [Fig. 13(d)] at the entire band for higher oblique incident angles. Notably, the present MS prototype does not aim to achieve wide-angle stability. Future work will focus on enhancing angular robustness, potentially beyond 60° or higher through structural miniaturization, reduced interlayer spacing, and single-layer design strategies.

V. EXPERIMENTAL VALIDATION

To verify the simulated results, the proposed MS containing 16 × 16 unit cells was fabricated on the FR4 substrate. The overall size of the prototype is 224 × 224 × 12.8 mm^3. Figs. 14(a) – 14(d) shows the top, middle, and bottom layers, and the assembled MS array prototype, respectively. The bandpass, LRCP conversion, and monostatic RCS characteristics were measured in a fully calibrated anechoic chamber under far-field conditions. Two identical linearly polarized horn antennas were utilized as a transmitter (T_x) and receiver (R_x) and connected to a vector network analyzer (VNA). Both T_x and R_x antennas are aligned in the same direction to capture the backscattered fields along the specular direction ($\theta = 0°$). The horn antennas were positioned at a far-field distance $d = 2D^2/\lambda \approx 2.4$ m to ensure uniform plane wave illumination on the fabricated prototype. Where D is the MS array dimension and λ corresponds to the highest operating frequency. To measure the cross-pol. reflections response, the antennas were positioned orthogonally in front of the MS to record the resultant reflected waves. For co-pol. reflection and bandpass responses measurements, antennas were aligned parallel. Figs. 15(a) – 15(c) illustrate the adopted experimental setups, respectively.

To obtain accurate results, a standard calibration procedure was employed. First, a same-sized copper plate was used as a reference to represent total reflection. Subsequently, a free-space measurement was performed (without placing the prototype) to account for free-space path loss values. The measured responses were first corrected by subtracting the free-space contribution and then normalized with respect to the PEC reference. The normalized reflection coefficient is expressed as: $\frac{\Gamma^{MS}-\Gamma^{FS}}{\Gamma^{PEC}-\Gamma^{FS}}$ where Γ^{MS}, Γ^{PEC}, and Γ^{FS} represent the measured responses of the MS, PEC plate, and free space, respectively.

The finalized measured results are plotted in Figs. 16(a) – 16(d), respectively. Fig. 16(a) indicates that the R_{yy} response stays below −10 dB from 3.8 to 5.2 GHz for bandpass and 5.75 to 7.4 GHz for LRCP conversion. Whereas corresponding R_{xy} magnitude stays above –2 dB only for the LRCP conversion band. From Fig. 16(b), the measured bandpass insertion loss appears closer to −2 dB from 3.8 to 5.2 GHz.

On the other hand, the T_{yy} magnitude is below −10 dB within the LRCP conversion band, indicating that the proposed MS facilitates high-efficiency LRCP transformation. Additionally, Fig. 16(c) shows a close match between the numerically evaluated and measured PCR responses. Furthermore, a comparison between simulated and measured RCS results for the proposed chessboard array is presented in Fig. 16(d), demonstrating that more than 10 dB of RCS reduction is achieved from 5.94 to 7.21 GHz, while no significant RCS reduction occurs in the transmission band. Notably, the measured results show excellent agreement with the simulation results; however, minor discrepancies are attributed to dielectric loss, fabrication tolerances, slight antenna misalignment, and finite-size effects.

Additionally, to highlight the proposed MS's novelty, the design was compared with the available literature listed in Table 1. The advantages of the proposed dual-functional MS can be compared to existing designs as follows:

1. The proposed MS design has more compact footprints than the designs reported in [17], [19], [20], [21], [22], [23], [24], [26], [28], and [29]. In addition, it is electrically thinner than the structures reported in [17], [18], [19], [20], [21], [23], [24], [26], [28], and [29].
2. The structural complexity of the proposed dual-functional MS is lower than that of the designs in [17], [18], and [19], as it avoids the use of lossy layers while preserving dual functionality. Furthermore, compared with [17], [18], [21], and [23], the proposed design incorporates fewer substrate layers.
3. In most prior studies, the reflection-mode performance is strongly dependent on the geometry of the integrated bandpass FSS layer. However, this dependency is effectively eliminated in the proposed design.
4. Finally, the proposed MS enables independent control of each functionality without introducing mutual performance degradation.

This comparative analysis demonstrates that available benchmark designs fall short of simultaneously and independently achieving the LRCP conversion and bandpass characteristics, which are distinctive key features of the proposed MS. Moreover, the proposed design maintains wideband RCS reduction only within the LRCP conversion band, thereby ensuring efficient and functionally independent operation.

TABLE 1. Proposed MS versus state-of-the-art benchmark designs.

Ref.	Pol.	Tx. (range) GHz, FBW %	10 dB LRCP conversion (range) GHz, FBW %	10 dB RCS reduction (range) GHz, FBW %	RCS Reduction Mechanism	Independency of reflection	Independent control of functionalities	Radome/ CCL Analysis	ML	UCS at λ_h^3
[17]	TE TM	Bandpass, (9.5 – 11.7), 20.7	NR	(3.3 – 8.5), 88.1 (15 – 20), 28.5 (2.8 – 20), 151	Lossy layer	No	No	No	5	0.5×0.5×1.01
[18]	Dual	Bandpass, (7.4 – 12.1), 48.2	(3.1–6.0), 63.73	(3.3 – 20), 143	Lossy layer	No	No	No	5	0.33×0.33×0.82
[19]	TE TM	Bandpass, (4.9 – 5.15), 4.97	NR	(1.32 – 17), 171.1 (1.4 – 16.8), 169.2	Lossy layer	No	No	No	3	1.8×1.8×0.59
[21]	Dual	Bandpass, (8.5 – 11), 25.6	(5.66–6.9), 19.74 (12.8–15.2), 17.14	(4.5 – 16), 112.2	LRCP Conversion	No	No	No	4	0.76×0.76×0.5
[22]	Dual	Bandpass, (3.9 – 4.3), 9.75	NR	(8 – 16), 66.6	Phase Cancellation	No	No	No	2	1.28×1.28×0.24
[23]	Single (TE)	Bandpass, (8.8 – 10.2), 14.7	NR	(4.8 – 10), 70.27 (11.1 – 17.2), 43.1	Phase Cancellation	No	No	No	4	0.49×0.49×0.46
[24]	Dual	Bandpass, 7.3 GHz and 12.6 GHz	NR	(4.2 – 13.9), 107.1	Phase Cancellation	No	No	No	2	0.74×0.74×0.35
[26]	Dual	Bandpass, 8.4 GHz	NR	(3.5 – 11.5), 106.6	Phase Cancellation	No	No	No	2	0.61×0.61×0.345
[27]	Dual	Bandpass, (11.3 – 13.3), 16.26	NR	(4.1 – 7.7), 61	Phase Cancellation	No	No	No	3	0.18×0.18×0.27
[28]	Dual	Bandpass, (3.7 – 4.3), 15	NR	(8.4 – 18), 72.7	Phase Cancellation	No	No	No	3	0.51×0.51×0.43
[29]	Dual	Bandpass, (11.8 – 12.1), 2.51	NR	(7.5 – 15.7), 70.7	Phase Cancellation	No	No	No	3	0.52×0.52×0.33
TW	**Dual**	**Bandpass, (3.74 - 5.12), 31.15**	**(5.72–7.33), 24.67**	**(5.94 – 7.21), 19.31**	**LRCP Conversion**	**Yes**	**Yes**	**Yes**	**3**	**0.34×0.34×0.31**

***UCS:** Unit Cell Size, **Pol.** polarization, **Tx.:** Transmission Behavior, **ML:** Metasurface Layers, $\boldsymbol{\lambda_h}$**:** Highest Operating Frequency, **TW:** This Work

VI. CONCLUSION

A novel three-layer MS has been proposed, designed, and experimentally validated to simultaneously achieve wideband LRCP conversion and high-efficiency bandpass transmission at adjacent frequency bands. Unlike previously reported dual-functional MS designs, whose reflection-mode performance strongly depends on the geometry of the integrated bandpass FSS layer, the proposed approach eliminates this dependency by incorporating diagonally rotated MSGs layers. This configuration enables efficient cross-polarization conversion in reflection while simultaneously maintaining high transmission transparency at out-of-band frequencies. To evaluate the transparency, an FSS incorporating a CD resonator is introduced in the middle layer. Simulation results predict that the resultant structure provides the LRCP conversion from 5.72 to 7.33 GHz (24.67%) with PCR exceeding 0.99, and the bandpass transmission covers the 3.74 – 5.12 GHz (31.15%) with simulated insertion loss of above −1 dB. Furthermore, when the proposed MS is arranged in a chessboard configuration using the 01/10 coding scheme, a monostatic RCS reduction exceeding 10 dB is achieved within the LRCP conversion band spanning 5.94 – 7.21 GHz, (19.31%). However, no noticeable RCS reduction is observed within the bandpass transmission region, confirming the independent operation of the two functionalities. Besides, the fabricated prototype experimentally validates the proposed dual-functional operating concept with acceptable agreement between simulation and measurement. Considering the combined and independent functionalities across distinct frequency bands, together with its low-profile configuration, the proposed MS is a potential candidate for Radome and communication applications, where simultaneous transmission and reduced scattering are highly desirable.

REFERENCES

[1] R. Teng, F. He, W. Hao, P. Wang, L. Gao, W. Xie, Z. Ye, J. Jiang, X. Ji, and L. Miao, "Enhanced high-gain antenna design with phase-controlled frequency selective rasorber for low-RCS performance," *IEEE Antennas Wireless Propag. Lett.*, vol. 23, pp. 4548–4552, 2024.

[2] M. Nasir, S. Koziel, and A. Iftikhar, "A miniaturized and high optically transparent frequency selective surface for RF shielding using double-glazed glass windows for green building applications," *IEEE Access*, vol. 13, pp. 18053–18062, 2025.

[3] N. Ullah, M. S. Islam, A. Hoque, A. Alzamil, M. S. Soliman, and M. T. Islam, "Design and development of a compact, wide-angle metamaterial electromagnetic energy harvester with multiband functionality and polarization-insensitive features," *Sci. Rep.*, vol. 14, no. 1, p. 19000, Aug. 2024.

[4] A. Paramanik, K. C. Venkata, and V. Subramanian, "A dual layer wideband angular stable frequency selective surface for linear to circular and circular to linear polarization conversion for 5G applications," *Sci. Rep.*, vol. 15, no. 1, p. 12059, Apr. 2025.

[5] W. Wang, Z. Fang, K. Tang, X. Wang, Z. Shu, Z. Zhao, and Y. Zheng, "Wideband gain enhancement of MIMO antenna and its application in FMCW radar sensor integrated with CMOS-based transceiver chip for human respiratory monitoring," *IEEE Trans. Antennas Propag.*, vol. 71, no. 1, pp. 318–329, Jan. 2023.

[6] W. Wang and Y. Zheng, "Wideband gain enhancement of a dual-polarized MIMO vehicular antenna," *IEEE Trans. Veh. Technol.*, vol. 70, no. 8, pp. 7897–7907, Aug. 2021.

[7] H. A. Khan, J. Zhang, S. Luo, and Y. Wang, "A single-layer checkerboard metasurface based on reconfigurable polarization converter for dual-mode RCS reduction," *IEEE Antennas Wireless Propag. Lett.*, vol. 24, pp. 2029–2033, 2025.

[8] S. Ghosh, P. M. Sainadh, A. Sarkhel, and S. Ghosh, "Wideband superstrate-loaded metasurface-based multifunctional polarization converters," *IEEE Antennas Wireless Propag. Lett.*, vol. 24, pp. 1337–1341, 2025.

[9] Q. Zheng, W. Liu, Q. Zhao, L. Kong, Y. Ren, and X. Yang, "Broadband RCS reduction, antenna miniaturization, and bandwidth enhancement by combining reactive impedance surface and polarization conversion metasurface," *IEEE Trans. Antennas Propag.*, vol. 72, no. 9, pp. 7395–7400, Sep. 2024.

[10] W. Yao, H. Gao, Y. Tian, J. Wu, L. Guo, and X. Huang, "Wideband low-RCS linear polarized array based on miniaturized polarization conversion metasurface," *IEEE Trans. Antennas Propag.*, vol. 71, no. 7, pp. 5663–5674, Jul. 2023.

[11] P. Wang, Y. Jia, W. Hu, Y. Liu, H. Lei, H. Sun, and T. J. Cui, "Circularly polarized polarization conversion metasurface-inspired antenna array with low RCS over a wide band," *IEEE Trans. Antennas Propag.*, vol. 71, no. 7, pp. 5626–5636, Jul. 2023.

[12] J. Liu, J.-Y. Li, and Z. N. Chen, "Broadband polarization conversion metasurface for antenna RCS reduction," *IEEE Trans. Antennas Propag.*, vol. 70, no. 5, pp. 3834–3839, May 2022.

[13] C. Fu, L. Han, C. Liu, Z. Sun, and X. Lu, "Dual-band polarization conversion metasurface for RCS reduction," *IEEE Trans. Antennas Propag.*, vol. 69, no. 5, pp. 3044–3049, May 2021.

[14] Y. Wang, Q. Xue, H. Xie, Z. Hu, and S. Liao, "Bandwidth enhancement in arrow-shaped polarization conversion metasurface under seven plasmonic resonances," *IEEE Antennas Wireless Propag. Lett.*, vol. 23, pp. 2254–2258, 2024.

[15] W. Feng, C. Li, Y. Wang, J. Chen, Y. Zhao, H. Arai, and K. Xu, "Single-/dual-band linear polarization converter with independently controllable passband and high selectivity," *IEEE Antennas Wireless Propag. Lett.*, vol. 23, no. 9, pp. 2713–2717, Sep. 2024.

[16] M. Yan, J. Wang, Y. Pang, C. Xu, H. Chen, L. Zheng, J. Zhang, and S. Qu, "An FSS-backed dual-band reflective polarization conversion metasurface," *IEEE Access*, vol. 7, pp. 104435–104442, 2019.

[17] L. Wang, S. Liu, X. Kong, Q. Yu, X. Zhang, and H. Zhang, "A multifunctional hybrid frequency-selective rasorber with a high-efficiency cross-polarized Passband/Co-polarized specular reflection band," *IEEE Trans. Antennas Propag.*, vol. 70, no. 9, pp. 8173–8183, Sep. 2022.

[18] L. Zhou and Z. Shen, "Hybrid frequency-selective rasorber with low-frequency diffusion and high-frequency absorption," *IEEE Trans. Antennas Propag.*, vol. 69, no. 3, pp. 1469–1476, Mar. 2021.

[19] F. Wang, Y. Wang, X. Zhang, L. Liu, K. Li, and Y. Ren, "Wideband low-RCS and gain-enhanced antenna using frequency selective absorber based on patterned graphene," *Sci. Rep.*, vol. 14, no. 1, p. 9306, Apr. 2024.

[20] Ş. Tahaimeci, B. Tütüncü, F. Bešlija, and L. Herceg, "Microstrip filters based on open stubs and SIR for high frequency and ultra-wideband applications," *J. Eng. Res.*, vol. 10, no. 3, pp. 212–223, Sep. 2022.

[21] L. Wang, S. Liu, X. Kong, H. Zhang, Q. Yu, Y. Wen, and D. Wang, "A multifunctional frequency-selective polarization converter for broadband backward-scattering reduction," *IEEE Trans. Antennas Propag.*, vol. 69, no. 5, pp. 2833–2841, May 2021.

[22] C. Huang, C. Ji, X. Wu, J. Song, and X. Luo, "Combining FSS and EBG surfaces for high-efficiency transmission and low-scattering properties," *IEEE Trans. Antennas Propag.*, vol. 66, no. 3, pp. 1628–1632, Mar. 2018.

[23] Y. Pang, Y. Li, B. Qu, M. Yan, J. Wang, S. Qu, and Z. Xu, "Wideband RCS reduction metasurface with a transmission window," *IEEE Trans. Antennas Propag.*, vol. 68, no. 10, pp. 7079–7087, Oct. 2020.

[24] M. Liao, X. Weng, W. Duan, K. Li, and M. Bi, "A broadband RCS reduction metasurface with dual transmission windows," *IEEE Antennas Wireless Propag. Lett.*, vol. 23, pp. 3113–3117, 2024.

[25] Y. Shang, X. Lei, C. Liao, and J. Chen, "Frequency-selective structures with suppressed reflection through passive phase cancellation," *IEEE Trans. Antennas Propag.*, vol. 68, no. 2, pp. 1192–1197, Feb. 2020.

[26] Y.-F. Fu, J.-D. Ji, Y.-J. Wang, F.-K. Zhou, C. Wang, and P. Chen, "Broadband radar cross section reduction binary metasurface with a high-efficiency intraband transmission window," *IEEE Antennas Wireless Propag. Lett.*, vol. 21, pp. 878–882, 2022.

[27] Q. Li, Y. Pang, Y. Li, M. Yan, J. Wang, Z. Xu, and S. Qu, "Low radar cross section checkerboard metasurface with a transmission window," *J. Appl. Phys.*, vol. 124, no. 6, Aug. 2018, Art. no. 065107.

[28] Q. Li, Y. Pang, M. Yan, J. Wang, Z. Xu, and S. Qu, "Reducing reflection of bandpass frequency selective surface using checkerboard surface," *J. Phys. D, Appl. Phys.*, vol. 51, no. 36, Aug. 2018, Art. no. 365103.

[29] B. Sima, K. Chen, N. Zhang, J. Zhao, T. Jiang, and Y. Feng, "Wideband low reflection backward scattering with an inter-band transparent window by phase tailoring of a frequency-selective metasurface," *J. Phys. D, Appl. Phys.*, vol. 55, no. 1, Oct. 2021, Art. no. 015106.

[30] N. Pouyanfar, J. Nourinia, C. Ghobadi, and V. Nayyeri, "A thin, wideband transmissive cross polarization converter," *Sci. Rep.*, vol. 15, no. 1, p. 3773, Jan. 2025.

[31] M. Yang, F. Lan, Y. Zhang, L. Qi, G. He, Y. Pan, T. Song, L. Wang, P. Mazumder, H. Zeng, and Z. Yang, "Collective-coupling enhanced ultra-broadband linear polarization conversion on zigzag-split metasurfaces," *IEEE Trans. Antennas Propag.*, vol. 71, no. 6, pp. 5001–5013, Jun. 2023.

[32] M. Chandra, Nilotpal, D. Samantaray, M. Thottappan, and S. Bhattacharyya, "A broadband transmissive type metasurface cross-polarization converter for EMC application," *IEEE Trans. Electromagn. Compat.*, vol. 65, no. 1, pp. 186–194, Feb. 2023.

[33] P. Xu, W. X. Jiang, S. Y. Wang, and T. J. Cui, "An ultrathin cross-polarization converter with near unity efficiency for transmitted waves," *IEEE Trans. Antennas Propag.*, vol. 66, no. 8, pp. 4370–4373, Aug. 2018.

[34] Y. Ge, C. Lin, and Y. Liu, "Broadband folded transmitarray antenna based on an ultrathin transmission polarizer," *IEEE Trans. Antennas Propag.*, vol. 66, no. 11, pp. 5974–5981, Nov. 2018.

[35] M. Nasir, S. Koziel, and A. Pietrenko-Dabrowska, "A multifunctional bi-anisotropic metasurface with reflection-transmission polarization conversion and narrow bandpass transmission characteristics," *Sci. Rep.*, vol. 16, no. 1, p. 13838, Mar. 2026.

[36] J. H. Shin and C. W. Jung, "Analysis of optical and microwave transmission by linewidth variation of metal mesh for FSS in GPTS," *IEEE Microw. Wireless Technol. Lett.*, vol. 34, no. 5, pp. 580–582, May 2024.

[37] S. Kosulnikov, F. S. Cuesta, X. Wang, and S. A. Tretyakov, "Molding of reflection and scattering from uniform walls using space-periodic metasurfaces," *IEEE Trans. Antennas Propag.*, vol. 72, no. 3, pp. 2992–2997, Mar. 2024.

[38] J.-S. Hong and M. J. Lancaster, *Microstrip Filters for RF/Microwave Applications*. Hoboken, NJ, USA: Wiley, 2001.

[39] M. A. Shukoor, S. Dey, and S. K. Koul, "Broadband chiral-type linear to linear reflecting polarizer with minimal bandwidth reduction at higher oblique angles for satellite applications," *IEEE Trans. Antennas Propag.*, vol. 70, no. 7, pp. 5614–5622, Jul. 2022.

[40] Y. Jia, Y. Liu, Y. J. Guo, K. Li, and S. Gong, "A dual-patch polarization rotation reflective surface and its application to ultra-wideband RCS reduction," *IEEE Trans. Antennas Propag.*, vol. 65, no. 6, pp. 3291–3295, Jun. 2017.
[41] H. Yang, T. Li, J. Liao, K. Gao, Q. Li, S. Li, and X. Cao, "Ultra-wideband low-RCS array antenna based on double-layer polarization conversion metasurface," *IEEE Antennas Wireless Propag. Lett.*, vol. 23, pp. 4069–4073, 2024.
[42] W. Wang, S. Yang, Z. Fang, Q. Sun, Y. Chen, and Y. Zheng, "Compact dual-polarized wideband antenna with dual-/single-band shifting for microbase station applications," *IEEE Trans. Antennas Propag.*, vol. 69, no. 11, pp. 7323–7332, Nov. 2021.
[43] M. Nasir, S. Koziel, and A. Iftikhar, "A highly miniaturized and wide angularly stable antenna-filter-antenna-based polarization rotating frequency selective surface for radar systems," *IEEE Access*, vol. 13, pp. 154729–154738, 2025.
[44] A. N. Serdyukov, I. V. Semchenko, S. A. Tretyakov, and A. H. Sihvola, *Electromagnetics of Bi-Anisotropic Materials: Theory and Applications*, vol. 11. Amsterdam, The Netherlands: Gordon and Breach Science Publishers, 2001.

MUHAMMAD NASIR received the B.S. and M.S. degrees in electrical engineering from COMSATS University Islamabad (CUI), Pakistan, in 2015 and 2020, respectively. He is currently pursuing the Ph.D. degree with the Department of Engineering, Reykjavik University, Iceland. His research interests include multilayer antennas array and metasurfaces.

SLAWOMIR KOZIEL (Fellow, IEEE) received the M.Sc. and Ph.D. degrees in electronic engineering from Gdańsk University of Technology, Poland, in 1995 and 2000, respectively, the M.Sc. degree in theoretical physics and the M.Sc. degree in mathematics, in 2000 and 2002, respectively, and the Ph.D. degree in mathematics from the University of Gdańsk, Poland, in 2003. He is currently a Professor with the Department of Engineering, Reykjavik University, Iceland. His research interests include CAD and modeling of microwave and antenna structures, simulation-driven design, surrogate-based optimization, space mapping, circuit theory, analog signal processing, evolutionary computation, and numerical analysis.

ANNA PIETRENKO-DABROWSKA (Senior Member, IEEE) received the M.Sc. and Ph.D. degrees in electronic engineering from Gdańsk University of Technology, Poland, in 1998 and 2007, respectively. Currently, she is an Associate Professor with Gdańsk University of Technology. Her research interests include simulation-driven design, design optimization, control theory, modeling of microwave and antenna structures, and numerical analysis.